Experimental and Computational Multiphase Flow
Vol. 5, No. 4, 2023, 381–395
https://doi.org/10.1007/s42757-022-0144-8

Experimental and numerical study of free-falling streams of particles impacting an inclined surface

David Dodds[1], Abd Alhamid Rafea Sarhan[1,2] (✉), Jamal Naser[1]

1. Department of Mechanical and Product Design Engineering, Swinburne University of Technology, Hawthorn, Victoria 3122, Australia
2. Department of Biomedical Engineering, The University of Melbourne, Carlton, Victoria 3010, Australia

Abstract

This paper presents a detailed experimental and numerical analysis of free-falling particle streams impacting a 45° inclined surface of differing materials. The particles used in this study were glass spheres with average diameters of 136 and 342 μm and a density of 2500 kg/m^3. The three mass flow rates considered are 50, 150, and 250 grams per minute (gpm). The effect of wall material on the collision process was also analysed. Special attention was paid to the influence of wall roughness. Therefore, a plate of stainless steel with polished surface, an aluminium sheet, and a Perspex plate with similar properties to those of the rest of the wall sections were used. The experimental data were used to improve and validate a wall collision model in the frame of the Lagrangian approach. A new drag force formula that includes the effects of particle concentration as well as particle Reynolds number was implemented into commercially available codes from CFX4-4 package. It was found that the improved CFD model better predicted the experimental measurements for the particle rebound properties. The rough-wall model in these results showed greater effect on smaller particles than on larger particles. The results also showed that the improved CFD model predicted the velocity changes slightly better than the standard model, and this was confirmed by both the quantitative velocity comparisons and the qualitative concentration plots. Finally, the inclusion of the particle–particle collision was shown to be the dominant factor in providing the dispersion of the particles post collision. Without a sufficient particle–particle collision model, the standard model showed all particles behaving virtually identical, with the main particle stream continuing after the collision process.

Keywords

CFD modelling
pneumatic conveying
particle diameter image analysis (PDIA)
particle–wall collisions

Article History

Received: 11 January 2022
Revised: 6 August 2022
Accepted: 15 August 2022

Research Article

1 Introduction

The Eulerian–Lagrangian approach to gas–particle flow modelling lends itself well to flows where the solid fraction is low enough to neglect any particle–particle interactions (Miao et al., 2019; Muhammad et al., 2019; Zhu et al., 2019). A number of industrial flows fall into this regime such as pneumatic conveying and mill duct flows within power stations (Raghav et al., 2018; Kabeel et al., 2019). In mill duct flows, as the whole solid volume fraction is quite low, the introduction of bends and complicated flow patterns can result in regions where a dense particle rope is formed, whose solid volume fraction suddenly increases so much that particle–particle interactions are no longer negligible (Li et al., 2018; Feng et al., 2020). Another major factor that heavily influences mill duct flows is the effect of particle–wall collisions (Manjula et al., 2017). The introduction of a rougher wall material considerably reduced the axial velocity profiles due mainly to the momentum transfer from the axial to the transverse direction (Ruiz-Angulo et al., 2019; Varaksin, 2019). Also, the increase in particle size resulted in a decrease of particle velocity due largely to the increase in relative slip velocity as mentioned previously. Due to experimental findings that the particle velocity is greatly influenced by such factors as mass loading, particle size, conveying air velocity, and wall roughness characteristics, to name a few, the number of numerical studies to increase prediction accuracy over the past 30 years is great. This has led to a

✉ Hamid.sarhan@unimelb.edu.au

Nomenclature

A	surface area of the particle
d_p	particle diameter
F_D	drag force
Γ	diffusion coefficient
m_p	particle mass
ϕ	variable quantity
Re_p	particle Reynolds number
ρ_g	gas density
S_ϕ, $S_{P\phi}$	source terms
$U_{p,g}$	velocity of particle and gas, respectively

Abbreviations

CFD	computational fluid dynamics
gpm	grams per minute
PIV	particle image velocimetry

number of proposed numerical models to better capture the trends seen in experimental works on horizontal two-phase pipe/channel flow (Sommerfeld and Huber, 1999; Kuerten and Vreman, 2016).

The connected papers by Sommerfeld (2003) and Sommerfeld and Kussin (2003) considered the effect of collision models, both particle–wall and inter-particle, of the transport of particles. The major findings of the work detailed how the inclusion of inter-particle models increased dispersion and resulted in lower stream-wise velocity. For a rough wall, a small increase in wall roughness leads to an increase in particle–wall collisions. In confined particle flows, it is inevitable that at some stages the particles will contact the bounding wall of the system. To accurately simulate particle flows, it is necessary to apply appropriate treatments for these collisions within CFD modelling. Many researchers have investigated these treatments. Sommerfeld (1992) identified some of the most important parameters in modelling particle–wall collisions, which are particle collision angle, particle translational and rotational velocities before collision, properties of the particle and wall materials, particle shape, and roughness of the wall surface. Due to the large number of variables that are in effect, there is a distinct lack of experimental results to allow detailed modelling of particle–wall collisions and consequently a deficiency in realistic numerical simulations.

In an attempt to further refine numerical simulations, the roughness of the wall has been taken into account. Matsumoto and Saito (1970) used an irregular bouncing model to explain the resuspending phenomenon observed in experimental results. Their model used a complicated sine function to describe the roughness of the wall. Although improved simulation results were achieved, the wall roughness formula was complicated and slightly ambiguous. Tsuji et al. (1985, 1987) considered particle interactions with rough walls in a different fashion. The method used in this approach introduced a virtual wall to replace the standard wall at impact angles smaller than 7°. The virtual wall has a randomly determined inclination to vary the rebounding angles of the colliding particles. The earlier study of Tsuji et al. (1985) investigated the effects of different sized particles in different sized pipes. The later work of Tsuji et al. (1987) extended the empirical relations of the previous work by investigating the effects of wall roughness for different values of inclinations. The results showed that increasing the inclination angle better simulated the experimental results, with more particles colliding with both the top and bottom walls, which was lacking in the previous study. The drawback of this method is that at collision angles greater than 7°, wall roughness is not accounted for. There are always effects of wall roughness regardless of approach angle, and hence this model failed to fully reproduce the results of experiments. Sommerfeld (1992) noted the shortcoming of Tsuji et al.'s works and made improvements by ensuring that a random wall inclination is included for all values of collision angle. The earlier work used a uniform distribution to determine the virtual wall inclination for all values of colliding angles. This model's predictions for the velocity fluctuations of the particle matched well with the experimental results (Miao et al., 2019).

Due to this constraint, Sommerfeld et al. (1993) performed experiments for further validation. By comparing different sized particles at various impact angles, results showed that smaller particles are affected more by the roughness of the wall. Also, at lower collision angles smaller than 35°, the rebounding angle tended to be greater than the incident angle. This is explained by the fact that at lower incident angles, the particle has a higher probability of hitting the tip of the roughness structures. Huber and Sommerfeld (1998) used Sommerfeld's previously developed rough wall collision model to predict particle flow through different configurations of pipes. The rough wall model tended to reduce the effect of gravitational settling and resulted in a considerable increase in pressure drop. Sommerfeld and Huber (1999) looked at the impact of individual particles of various materials impacting different surfaces with varying roughness. The particles considered contained both spherical glass beads and slightly non-spherical quartz particles. The findings

of the experimental work were utilised to better define the numerical simulations through the particle–wall collision model. The main findings of the work were that both wall roughness and sphericity of the particles provide a slight scattering of the rebounding particles. Sommerfeld and Kussin (2004) utilised the developed rough wall model to consider horizontal pipe flow, concentrating their focus on wall material, particle size, and mass loadings. The results showed that the greater the wall roughness, the higher the momentum loss and the subsequent increase in both slip velocity and pressure drop. Also, angular velocity was found to be a key parameter in the wall collision process, but due to the lack of reliable measured data, this has yet to be validated.

Although many researchers have already studied experimentally and computationally the particle–wall collision process (Dodds et al., 2020a, 2020b), this work was completed to gain additional knowledge of the behaviour of particle streams impacting a 45° inclined surface of differing materials. The focus of this study is to quantify the behaviour of particle streams under differing mass flow rates and particle sizes. The effects of mass flow rates will also be investigated to discover whether the average particle is strongly influenced by the mass flow rate. Two different particle sizes were then used to establish whether wall material roughness has a significant role when considering streams of particles as opposed to individual particles. The idea of validation using previously reported data by other researchers significantly limits the number of parameters that can be considered. The experimental study may not be ground-breaking, but has been invaluable for testing the improvements made to CFD models and also extends the knowledge base for the behaviour of particle streams which behave distinctly different to individual particles.

2 Experimental setup and material

2.1 Particle image velocimetry (PIV)

PIV is used to visualise 2D flows of fluid or particle motion. The main theory of PIV is to seed the fluid flow with particles, which are then illuminated so that a recording device can obtain a digital image at specified time intervals from which motion of the particles can be determined (see Fig. 1) (Afshar et al., 2018; Raghav et al., 2018; Luo et al., 2019). The seeding particles are dependent on the type of flow to be considered.

In PIV systems, lasers are typically used because of their ability to produce high energy light over a very small wavelength range which can be formed into a stable sheet of light. Lasers allow the light to be of a single wavelength, which reduces the color aberrations when illuminating and

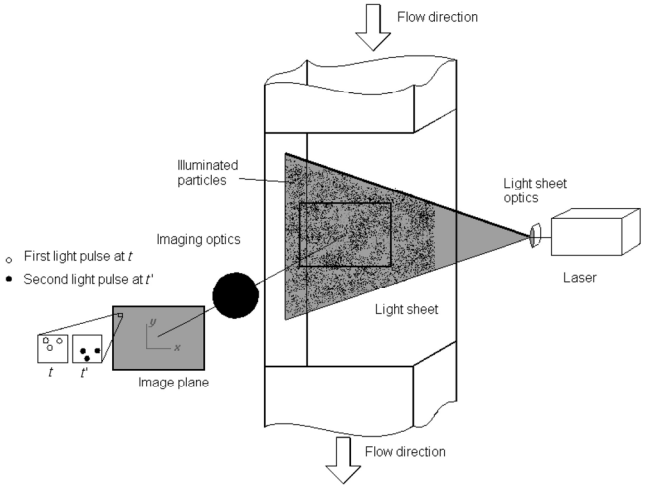

Fig. 1 Particle diameter image analysis (PDIA) experimental setup.

recording the particles. For this experiment, a Neodym-YAG laser was used, which produced a light sheet at a wavelength of 532 nm. The timing of the laser and camera is connected to pulse the laser only when an image is to be recorded. The pulse for this experiment was set to 0.25 s, allowing for 4 pairs of images per second to be recorded. Once the particles are sufficiently illuminated, the flow is ready to be measured. There are two main approaches to capture the fluid flow images, which are single-frame/multi-exposure and multi-frame/single-exposure. These techniques are highlighted in Fig. 2. As the name suggests, the single-frame method captures the particle motion on a single image. The principle difference between the two methods is that with the single-frame method, the temporal order of the particle motion is unclear and as such the direction of motion is ambiguous. In fluid flow whereby the fluid motion is quite predictable and the general direction is known, the single-frame method is quite appropriate, but when motion is quite unsteady and erratic, then the multi-frame method is likely to produce greater accuracy due to the temporal and spatial information acquired.

The fluid flow image is captured using a CCD camera with a light sensitive area of pixels that converts light into a digitized form which can be easily stored in a computer. The advantage of using a digitized form of image is that the camera speed is only restricted by the speed at which the camera can store the digital image to the memory buffer. The flow is analyzed by considering the movement of the seeding particles between two consecutive frames knowing the time interval. The particle movement was described in integral form by Westerweel (1997):

$$D(X;t,t+\Delta t)=\int_{t}^{t+\Delta t} v(X(t),t)\mathrm{d}t \tag{1}$$

where $v(X(t), t)$ is the tracer particle velocity and Δt is the

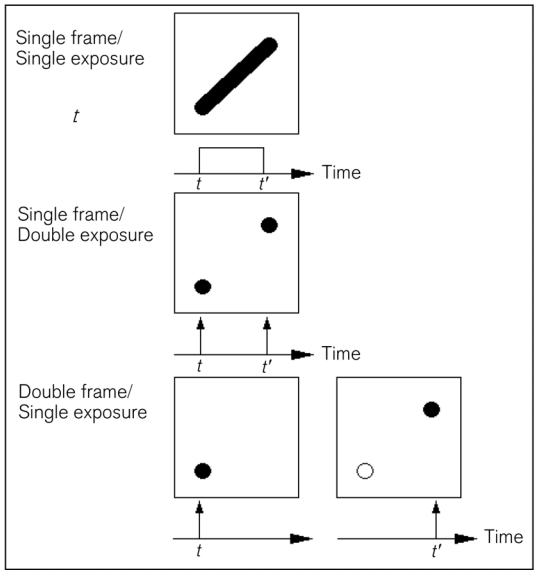

Fig. 2 PIV exposure techniques.

time interval between two images. As PIV images can contain many particles, the image is broken up into a number of interrogation windows and the spatial averaging of particle movement within a given window is calculated. As the values are averaged for given cells, for fluid flows, which are quite steady in nature, several image pairs can be analyzed to give more statistically accurate results. Time dependent and erratic flows may need to be analyzed on a frame-by-frame basis to capture fluid motion.

2.2 Experimental study conditions

The experimental setup shows the apparatus used for the study (see Fig. 3). A particle feeder releases particles via the inlet tube and allows them to free-fall and impact against a 45° inclined plate. The plates are interchangeable to test the effects of different rebound materials on the behaviour of the particle streams.

The rig was constructed of clear Perspex walls to allow the transmission of the laser sheet and to allow for the image to be captured by the camera. The experimental procedure used for this study is PIV whereby paired images, captured by photographing particles moving through a laser sheet, are analyzed to create a 2D vector plot of particle movement. The camera, triggered by a pulsing laser, can capture up to four pairs of images every second. Averaging numerous pairs of images generates a time averaged flow field. The basic steps of PIV are as follows:

- Seeding the flow with particles to scatter light for data recording.
- Illumination of a plane with a pulsed light.
- Recording of the image with enough resolution to distinguish individual particles.
- Analysis of the image by dividing the illuminating plane into very small regions and calculating the average displacement of the particles in each region.
- Post-processing to remove the obviously erroneous vectors.

In total, 18 different conditions were tested using the current experimental configuration. The 18 cases were combinations of two different particle sizes, three different rebound materials, and three different flow rates. The particle diameter ranges were 106–212 μm (average of 136 μm) and 300–425 μm (average of 342 μm). The particles used were solid glass spheres with a density of 2500 kg/m^3, and the sphericity was not considered in this study. The rebound materials consist of a Perspex plate with similar properties to those of the rest of the wall sections, an aluminum sheet considered to be a machined surface (not highly polished), and a plate of stainless steel with a highly polished surface finish. The three mass flow rates considered were 50, 150, and 250 grams per minute (gpm). These feed rates were constantly monitored by a variable feeding system, which ensured variation of less than 5%.

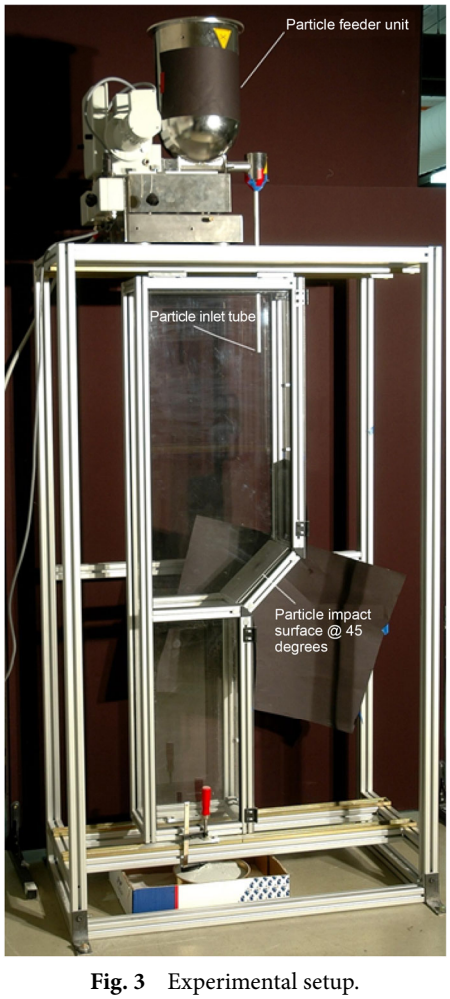

Fig. 3 Experimental setup.

3 Mathematical models

The simulations in this section are about gravity driven particle flows where particles are released into an initially still domain. As the particle flow is continuous, the once still air is entrained by the particle stream until terminal velocities are reached. The major forces at play in this case are gravity that pulls particles downward and the drag force between the particle and the slower moving air. The low particle-fraction (PF)-to-gas ratio lends itself ideally to the Eulerian–Lagrangian approach. Under the Eulerian–Lagrangian approach, the gas and PF are treated as interacting phases. The simulation carried out throughout this study was undertaken using the commercially available CFD software CFX4-4.

3.1 Gas phase model

The continuous gas phase is calculated using the Navier–Stokes equations for which the general form can be written as

$$\frac{\partial}{\partial t}\left(\rho_{\mathrm{g}}\phi\right)+\frac{\partial}{\partial x_i}\left(\rho_{\mathrm{g}}U_i\phi\right)=\frac{\partial}{\partial x_i}\left(\Gamma\frac{\partial\phi}{\partial x_i}\right)+S_\phi+S_{\mathrm{P}\phi} \tag{2}$$

where ρ_{g} is the gas density, U_i is the velocity vector, i is the unit vector, ϕ is the variable quantity, Γ is the diffusion coefficient, S_ϕ is the source term for the gas phase, and $S_{\mathrm{P}\phi}$ is the additional source term due to the interaction between the gas and the PF. Depending on ϕ, Eq. (2) represents mass, momentum, species, or energy conservation. For conservation of mass, $\phi = 1$, and when $\phi = U_i$, then Eq. (2) becomes the momentum equation. The standard k–ε two-equation turbulence model was used to close the Navier–Stokes equations.

3.2 PF phase model

The Lagrangian particle tracking method is used to calculate the individual trajectories of the dispersed PF phase. Equating the PF inertia with external forces, the momentum equations can be described by the general equation in Eq. (3):

$$\frac{\mathrm{d}\vec{u}_{\mathrm{p}}}{\mathrm{d}t}=F_{\mathrm{D}}\left(u_{\mathrm{p}}-u_{\mathrm{g}}\right)+\frac{\vec{g}\left(\rho_{\mathrm{p}}-\rho_{\mathrm{g}}\right)}{\rho_{\mathrm{p}}} \tag{3}$$

The left side of the equation describes the inertia of the particle phase while the right side describes the external forces acting upon the particle phase. F_{D} denotes the drag force between the particle and the gas phase and is equated using the Schiller–Naumann correlation for a spherical particle. The second term on the right-hand side denotes the gravitational force calculated based on the density difference between the PF and gas phase. Although other forces may also influence the particle trajectory, the drag and gravitational are the predominant forces acting on the PF in mill duct flows.

3.3 Drag force model

The drag force generally takes the form:

$$F_{\mathrm{D}}=\frac{1}{2}A_{\mathrm{CS}}\rho C_{\mathrm{D}}\left|V_{\mathrm{Rel}}\right|V_{\mathrm{Rel}} \tag{4}$$

where A_{CS} is the cross-sectional area perpendicular to the velocity direction, ρ is the density of the continuum medium, V_{Rel} is the relative velocity between the particle and the continuum phase, and C_{D} is the coefficient of drag of the particle. The standard model by Clift et al. (1978) employed by CFX4-4 is given by

$$C_{\mathrm{D}}=\frac{24}{Re}\left(1+0.15Re^{0.687}\right) \tag{5}$$

where

$$Re=\frac{\rho\left|V_{\mathrm{Rel}}\right|d}{\mu} \tag{6}$$

Here, d is the particle diameter, ρ is the fluid density, and μ is the viscosity. The drag coefficient only relates the amount of drag to the relative velocity. For extremely dilute flows whereby the particles are well dispersed, this relation is adequate, but when the volume fraction of particles increases, the effect of neighbouring particles cannot be excluded. This study includes the development of a new particle drag coefficient formula considering the effect of neighbouring particles on the drag force particles entrained in particle streams. The improved drag coefficient is given by

$$C_{\mathrm{D}}=\frac{24}{Re}\left[1+0.15Re^{0.687}+0.000353\left(\log\left(\sqrt[3]{\frac{\pi}{6\alpha}}\right)\right)^{15.93}-0.16\left(\log\left(Re\right)\right)^{3.62}\right] \tag{7}$$

where α is the particle volume fraction within the given cell.

3.4 Particle–wall collision model

The standard particle–wall collision based on the work of Shuen et al. (1985) included in CFX4-4 consists of a particle being reflected off the wall surface based on the coefficient of restitution. This coefficient is a direct measure of the amount of energy lost during the collision process and effectively reduces the normal velocity of the rebounding particle. Figure 4 shows the relationship between the pre- and post-collision velocities, both parallel and normal to wall.

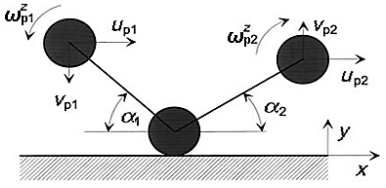

Fig. 4 Configuration of a particle–wall collision.

To model particle–wall collision, a rough-wall collision model similar to that of Sommerfeld (1992) was implemented. This model considers the effect of slight undulations on the wall surface. These slight undulations result in slightly modified impact angles by introducing a virtual wall as seen in Fig. 5.

The calculation for post-collision velocities is approached the same way as normal wall, but the incoming velocities are adjusted to incorporate the slight impact angle change. The formulas to calculate the post-collision velocities for both sliding and non-sliding collisions are as Eqs. (8)–(11).

Non-sliding collision:

$$u_2 = \frac{5}{7}u_1 \tag{8}$$

$$v_2 = -ev_1 \tag{9}$$

Sliding collision:

$$u_2 = u_1 + f_d(1+e)v_1 \tag{10}$$

$$v_2 = -ev_1 \tag{11}$$

where u_1 and u_2 represent the corresponding velocities pre- and post-collision in the tangential direction with respect to the collision, v_1 and v_2 are the velocities normal to the wall, e is the coefficient of restitution between the two particles, and f is the coefficient of friction. A non-sliding collision occurs when the condition in Eq. (12) is valid:

$$|u_1| \le \frac{7}{2} f_0 (1+e) v_1 \tag{12}$$

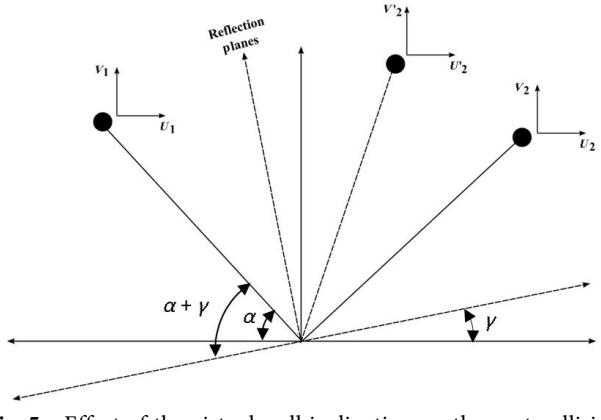

Fig. 5 Effect of the virtual wall inclination on the post-collision properties.

The equations for the standard model and improved are identical, but the incoming velocities for the improved model have been modified according to the roughness angle based on the work of Sommerfeld (1992).

3.5 Particle–particle collision model

The standard CFX4-4 software package does not account for particle–particle collision as part of the Lagrangian framework. As a consequence, the software needed to be modified to consider the effect of particle collisions through different flow systems. The modelling method implemented into the program is based on the model developed and refined by Sommerfeld (2001). The basis of this method is the creation of a fictitious particle that is used for the calculation of collision probability and, if required, the collision process.

As the Lagrangian particles are tracked individually through the flow domain, sampling the average particle velocities through a particular computational cell creates a fictitious particle. With the fictitious particle created, the collision probability of collisions occurring between the tracked and fictitious particles is calculated using a similar method for that of the kinetic theory of gases. The formula for the collision probability is as Eq. (13) (Sommerfeld, 2001):

$$P_{\text{coll}} = \frac{\pi}{4}\left(d_{\text{p,real}} + d_{\text{p,flict}}\right)^2 \left|\vec{u}_{\text{p,real}} + \vec{u}_{\text{p,flict}}\right| n_{\text{p}} \Delta t \tag{13}$$

where d is the diameter of the relevant particle, u the velocity of the relevant particle, n_{p} the number of particles per unit volume, and Δt the time step. After the collision probability is calculated, this probability is compared with a random number (RN) that is generated. A collision is to be simulated if the generated RN is less than P_{coll}. When a collision is to be simulated, the location of collision point on the real particle is determined randomly and the resulting post-collision velocities are calculated using Eq. (14) (Jain et al., 2019):

$$u_1' = u_1 \left(1 - \frac{1+e}{1+\frac{m_1}{m_2}}\right) \tag{14}$$

where u_1 and u_1' are the pre- and post-collision velocities respectively in the tangential direction relative to the collision vector between particle centers at the time of impact, and m_1 and m_2 are the respective masses. In the normal direction, during the collision process, a particle may be sliding against the wall surface or, depending on the friction between the surfaces, the particle may rotate in a non-sliding collision. The effects of the two sliding conditions are accounted for by Sommerfeld (2001, 2003).

Non-sliding collision:

$$v_1' = v_1\left(1-\frac{\frac{2}{7}}{1+\frac{m_1}{m_2}}\right) \tag{15}$$

Sliding collision:

$$v_1' = v_1\left[1-f(1+e)\frac{u_1}{v_1}\frac{1}{1+\frac{m_1}{m_2}}\right] \tag{16}$$

where m_1 and m_2 are the respective masses of the considered particles.

4 Boundary conditions and model properties

The geometry of this model is based on the dimensions of the experimental rig discussed earlier in Section 2.2. The geometry domain contains three main sections: the upper region where the particles are released into, the middle impact region where the main particle–wall collision takes place, and the lower section where the particles exit the domain. To obtain an acceptable accuracy with acceptable computational time, various grid independency tests were conducted with different mesh resolutions. Different grids of the model were generated using the FAME Hexa meshing technique where each grid has a similar meshing scheme. To evaluate the impact of the grid on the results, simulations were carried out on all grids. It has been verified that the change in the solution in the cases with higher mesh resolution is small. Also, it was found that there were no significant differences in the results. Figure 6 shows the configuration of the mesh for the geometry. The focus of this section is to highlight the influence of particle–wall collision models and in particular the rough-wall characteristics on the average movement of streams of particles. And as such the refinement of the grid revolves around the middle impact section, as this is where the most accurate results are required. Due to the structured mesh solved in CFX4-4, the refinement in middle section is carried through and adversely affects the other regions.

In the experimental setup, the rig was open to atmospheric pressure both at the top and bottom surfaces so the CFD model was given pressure boundaries of zero static pressure. Mass flow is free to enter and leave the domain when necessary. Particles are released into the domain at a similar point in the CFD model as in the experimental study. The particles enter through a user 2D patch and are given a velocity profile based on the location and velocity measured

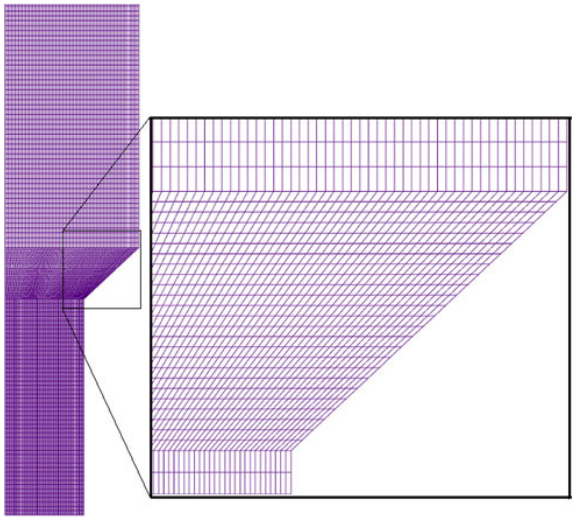

Fig. 6 Mesh configuration for the present CFD geometry.

in the experimental study; therefore, the quantities slightly vary for all cases. All the wall sections have a no-slip boundary condition applied to the continuous phase or in this case, the air. As mentioned earlier, the treatment of the particle interaction with the wall is the focus of this study and varies according to the wall model used.

5 Numerical simulations

To investigate the many aspects of this study, a number of simulations were run and compared. The first part of this section looks at the influence of the drag force model and turbulent dispersion on the flow characteristics of the particle just prior to impacting the angled wall. To investigate the influence of the drag model, the two different drag model approaches looked at were:

- The standard drag model using the coefficient of drag based on Eq. (5), as a function of particle Reynolds number only.
- The new drag model, Eq. (7), calculating the coefficient of drag based on particle Reynolds number and particle concentration.

Each of these models was simulated with the turbulent dispersion model first switched on and then turned off. The turbulent dispersion model simply adds in a fraction of random velocity to the particle based on the turbulent energy of the fluid within a given computational cell. Summary of simulation conditions for the various cases is given in Table 1.

Due to the importance of the wall collision modelling in this section, a brief overview of the modelling procedure will now be discussed. When a particle impacts a solid surface, whether it is a fixed wall or even another particle, energy is lost in the form of noise, heat, and deformation.

Table 1 Summary of simulation conditions for the various cases

Case	Simulation condition
Simulation 1	Standard model
Simulation 2	Simulation 1 with turbulent particle dispersion
Simulation 3	Simulation 2 with improved particle inlet velocity profile
Simulation 4	Simulation 3 with new drag force model
Simulation 5	Simulation 4 with rough-wall particle collision model
Simulation 6	Simulation 4 with particle–particle collision model
Simulation 7	Simulation 4 with rough-wall particle collision model and particle–particle collision model (improved)

The modelling of this process is introduced through the use of a coefficient of restitution, which differs depending on the materials colliding. Not only are the materials considered important, other influences on the coefficient of restitution are not to be neglected as well, such as the impact velocity, particle size, and impact angle. Due to the large number of variables required for the coefficient of restitution, typical values for the appropriate collisions to be modeled in this section have been taken from various sources in the available literature. The coefficients of restitution for glass beads impacting the three surfaces were assumed to be 0.9 for the stainless steel, 0.7 for the polyvinyl chloride (PVC), and 0.5 for the aluminum. These were assumed based on the experimental work of the researchers: Grant and Tabakoff (1975), Sommerfeld and Huber (1999), Sommerfeld (1992, 2001, 2003), Joseph et al. (2001), and Gondret et al. (2002). According to the work of Sommerfeld (1992) and Joseph et al. (2001), the typical value of surface roughness for the materials used is between 5 and 20 μm. Based on these roughness values, the following angle variations have been assumed: for the stainless steel with highly polished surface, an angle change of ±1.4° was used; for the PVC surface as Joseph (2003) compared closely to a non-polished steel surface, ±2.5° was used; for the unpolished aluminum surface, an angle change of ±3.5° was assumed. The roughness component or angle change is introduced through a random number to slightly modify the impact angle of the rebounding particle as discussed earlier.

6 Results and discussions

Figure 7 shows a typical PIV image from the experimental work. Whenever a particle crosses the laser sheet, the camera captures the scattered light, producing a representation of particle location at a particular instant. The brighter regions represent higher particle concentrations. A pseudo-relative particle concentration plot is determined by analyzing the individual images and determining for each pixel how many times a particle was present. Using MATLAB, the individual images were converted to a light intensity map

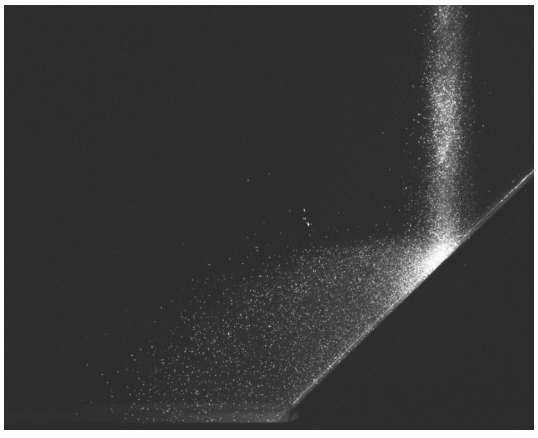

Fig. 7 Sample of PIV images obtained in the present work.

based on the grayscale image. On a grayscale image, the scale ranges from 0 for black to 256 for white. It was determined through trial and error that the threshold to recognize the particles was a grayscale value of 150. Using this threshold value, pixels containing a light intensity greater than 150 were given a value of 1, and less than 150 were given 0. This procedure reduced any background effects due to imperfect images. Therefore, for the 800 images analyzed, an averaged image with values from 0 to 800 was conceived giving a relative particle concentration plot. It is not possible to convert this scale to quantitative values, so any conclusion drawn from these comparisons will only be qualitative.

Figure 8 shows the results of the average concentration plots for the larger particles at the highest flow rebounding off aluminum, PVC, and stainless steel. The areas of lighter color are the regions where particles collided more often. As would be expected, the lightest shading for all the cases shown represents the region on the inclined wall where the majority of particles fall. Although direct quantitative values for the particle concentrations are not available in this method, the results can directly be qualitatively compared with CFD.

Figures 9–11 show the average velocity vectors for the particle phase plotted on top of the absolute velocity contours. The plots show the large particles at a rate of 250 gpm rebounding off the three different materials. In the case of the aluminum surface in Fig. 9, the maximum absolute particle velocity is achieved within the core region of the particle stream just before the wall collision. After the collision, the absolute particle velocities drop by about 35%, but this is to be expected due to the energy consumed within the collision process. The velocity vectors show an interesting trend, with the upper vectors having less horizontal component of the velocity. In a perfect elastic collision between a spherical particle and a 45° inclined wall, the resulting exit velocity would be horizontal in the immediate region after collision. As the particles move away

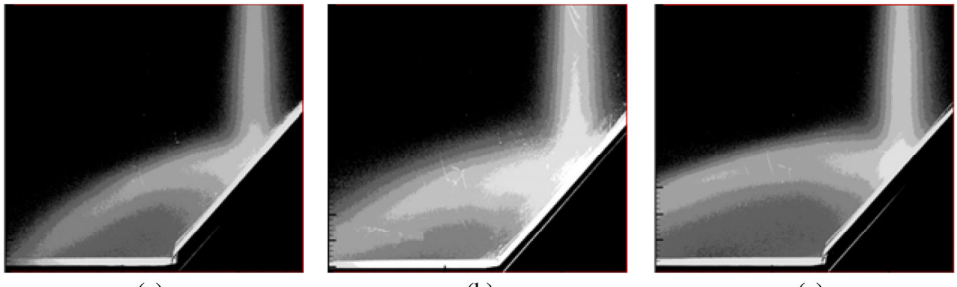

Fig. 8 Averaged particle concentration plots for 342 μm particles at a flow rate of 250 gpm rebounding off (a) aluminium, (b) PVC, and (c) stainless steel.

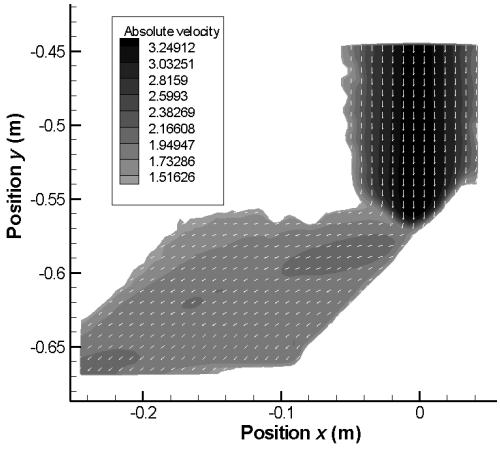

Fig. 9 Velocity contour and vector plot for the large particles at the highest flow rate impacting the aluminium surface.

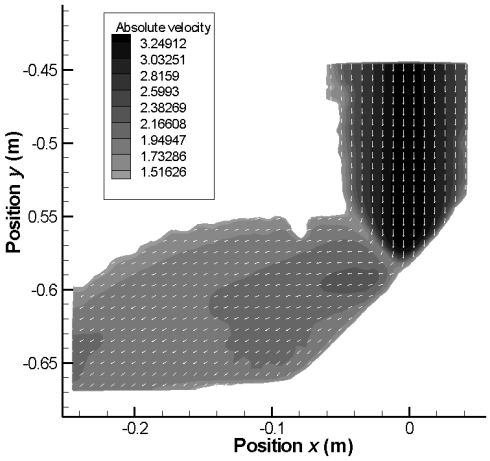

Fig. 10 Velocity contour and vector plot for the large particles at the highest flow rate impacting the PVC surface.

from the wall, gravity would impart a downward component to the particles' motion.

Due to the coefficient of restitution, a part of the normal component of particle velocity with respect to the wall is lost and this is seen in the velocity vectors. The results show that along the surface of the wall, the velocity vector angles mimic those of the wall, suggesting that a number of

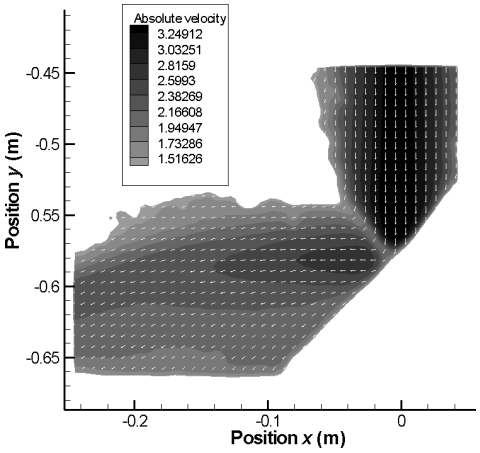

Fig. 11 Velocity contour and vector plot for the large particles at the highest flow rate impacting the stainless steel surface.

particles are travelling along the wall surface. The particles that find themselves in the lower region near the wall are generally those particles that have lost a majority of their momentum through a combination of wall collisions and inter-particle collisions. Particles to the right of the core in the particle stream have a lower absolute velocity to begin with because of the exposure to the slower moving air. These slowly moving particles are also the first to collide with the wall surface, giving them a horizontal velocity while the bulk of the freefalling are still falling downward. This difference in velocity direction results in repeated collisions with both the wall and other particles. Once trapped in this cycle, the trapped particles find it difficult to remedy the situation and generally follow the wall surface. This combination of wall and inter-particle collisions explains the spread of the particles in the post-wall-collision region. If no particle–particle collisions were to occur, the post-collision particle stream would almost mirror the stream before impact, but it is clear that this is not the case, so it is obvious that the influence of inter-particle collision has significant effect to the post-collision particle motion.

The results for the case of the same particle conditions impacting the PVC surface are shown in Fig. 10. Although

the incoming velocities were very similar to the aluminum case, the post-collision velocity contours show a distinct increase in absolute velocity, and the velocity vectors show a more horizontal velocity post collision. This velocity direction would suggest that coefficient of restitution for the PVC is higher than that of the aluminum surface, which is also highlighted by the extended distance the particle stream achieves. This was confirmed by the findings of Grant and Tabakoff (1975), which suggested that the mean normal coefficient of restitution of glass particles on aluminum, at low collision angles, varies between 0.4 and 0.6. Compared with the findings of Sommerfeld and Huber (1999) where the coefficient of restitution of glass particles on PVC was found to be approximately 0.7, a similar trend is seen with both the post-wall-collision spread of particles and the velocity vectors travelling along the wall surface, again suggesting the presence of particle–particle collisions.

The stainless steel surface produced a particle stream with the greatest post-collision absolute velocity (see Fig. 11). This suggests that the coefficient of restitution was higher than those of the other surfaces. This is consistent with findings of other researches on the particle–wall collisions. The resulting horizontal velocity vectors suggest that the coefficient of restitution would be equal to 1, which would imply that almost no energy is lost through the collision process, which is not possible due to energy lost through noise, heat, and deformation. As a coefficient of restitution equal to 1 is impossible, the results suggest that the wall roughness and particle–particle collision must influence the horizontal velocity achieved.

Considering the normalized horizontal velocity profiles shown in Fig. 12, the mass flow rate for the large particles impacting the stainless steel surface shows very little difference. The results shown are velocity profiles that have been normalized against the relevant incoming velocities. This would suggest that although the different mass flow rates produced similar normalized velocities, the absolute velocity for the higher mass flows would be larger, corresponding to the incoming velocity. For the large particles rebounding off the stainless steel surface, it is interesting to see that post-collision velocities produce similar results. This finding suggests that the coefficient of restitution is independent of mass flow rate.

Figure 13 shows a similar trend for the case of large particle impacting the PVC surface. Again, the peak normalized velocities for the three mass flow rates are very similar, suggesting that any absolute velocity difference is a product of the incoming velocity and not of the wall collision process.

For the cases of the smaller particles, the similarity for the two presented cases is not as profound as in the large particle cases, but the trend is still evident. For the PVC surface shown in Fig. 14, the normalized velocities were very similar, again suggesting that the smaller particles were behaving similarly to their larger counterparts. For the case of the stainless steel surface, as seen in Fig. 15, the difference in the normalized velocity results is slightly more profound. Due to the fact that the peaks are in the same region, the authors believe that the mass flow is not directly responsible for the discrepancy in the results.

It is evident that the highest flow rate of the smaller particles produced the lowest peak normalized velocities, which would suggest that more energy is lost throughout the collision process. This additional energy loss is more likely to be caused by additional particle–particle collisions,

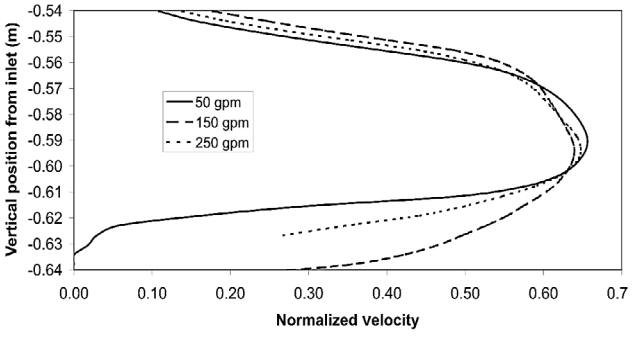

Fig. 13 Normalized horizontal velocities of the large particles rebounding off the PVC surface.

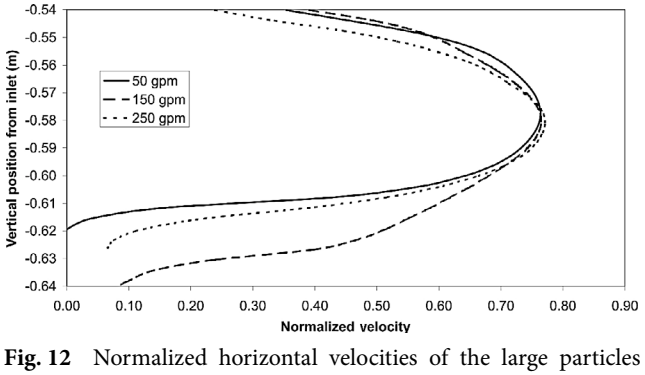

Fig. 12 Normalized horizontal velocities of the large particles rebounding off the stainless steel surface.

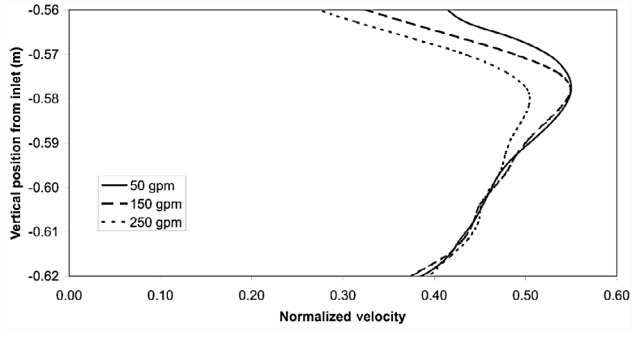

Fig. 14 Normalized horizontal velocities of the small particles rebounding off the stainless steel surface.

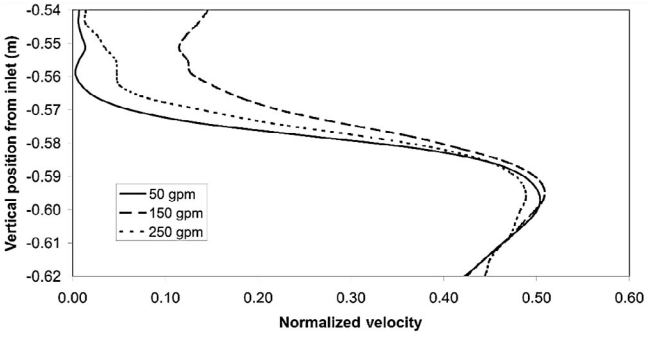

Fig. 15 Normalized horizontal velocities of the small particles rebounding off the PVC surface.

and due to the fact that at smaller diameter, the number of particles for a given mass flow rate increases significantly, the number of particle–particle collisions would also increase greatly. This would explain why the results differ between the different particle sizes. The number of smaller particles for a given mass flow rate is much bigger, so the incoming velocity for the smaller particles is much higher with respect to their natural terminal velocity, the particles collide with the wall and now endure an increased amount of drag force, and the particle velocities drop significantly, resulting in a perceived reduction in restitution coefficient.

As touched on in the previous section, it is evident that the size of particles does have a large bearing on the particle behavior. For a given mass flow rate of particles, the particles with the lower average diameter or size range will greatly outnumber their larger averaged diameter range counterparts. A greater number of particles will result in a greater chance of particle–particle collisions, particularly during the wall collision process when the particles are all heading in different directions. An increase in particle–particle collisions results in a loss of energy during the collision process which equates to lower normalized velocities in Figs. 14 and 15. Also as explained before, the smaller particles experience greater assistance from the particle wake phenomenon, and after collision process the change of direction results in lower assistance from the airflow, which causes a sudden rise in drag force, resulting in lower post-collision velocities.

Figure 16 shows the concentration plots for the small particles at a flow rate of 250 gpm. The incoming stream's size and color would suggest that the properties before the wall collision were virtually identical for all the surfaces, so the after-collision properties will show the difference between the rebounding surfaces. The aluminum surface provided a small fanning of the particles post collision, which would suggest a lower coefficient of restitution for the aluminum compared to the other surfaces. PVC provided the next biggest particle spread with the stainless steel surface providing the largest spread and consequently displaying the highest coefficient of restitution. Figure 17 shows the trend in a slightly different way. The peak normalized horizontal velocities show that the amount of energy lost during the wall collision with the aluminum surface is greater than the other cases, suggesting that the coefficient of restitution is lower. This is consistent with the findings shown in the concentration plots.

The results for the different surfaces with the larger particles at a flow rate of 150 gpm display similar findings to those of the smaller particles. Again, the aluminum surface resulted in smaller normalized velocities and shorter mean particle travel distance (see Fig. 18). The reverse is seen with the stainless steel surface, as shown in Fig. 19 with larger normalized horizontal velocity and a mean particle stream that travels further in the horizontal direction, which is in good agreement with the findings of the smaller particle case. The numerical results are validated against the experimental findings, consisting of quantitative data for the normalized velocity components where there can

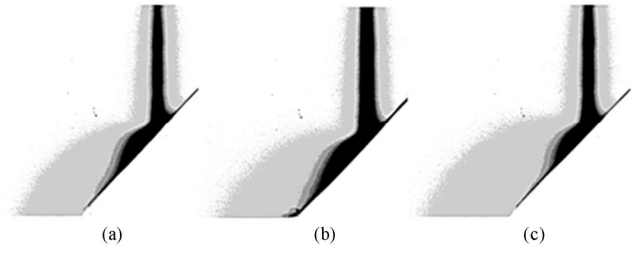

Fig. 16 Particle concentration plots of the small particles at a flow rate of 250 gpm rebounding off (a) aluminum, (b) PVC, and (c) stainless steel.

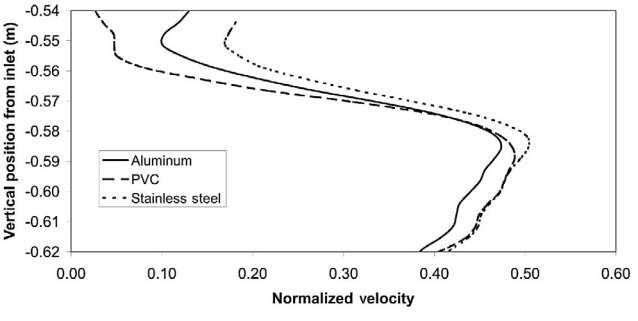

Fig. 17 Normalized horizontal velocities of the small particles at a flow rate of 250 gpm.

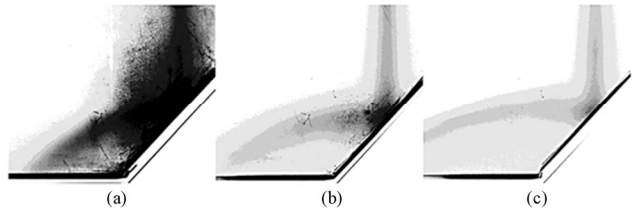

Fig. 18 Particle concentration plots of the large particles at a flow rate of 150 gpm rebounding off (a) aluminum, (b) PVC, and (c) stainless steel.

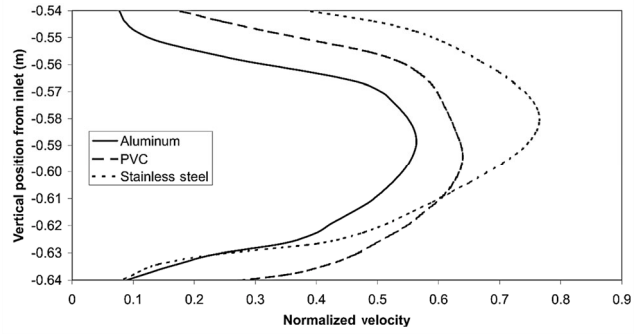

Fig. 19 Normalized horizontal velocities of the large particles at a flow rate of 150 gpm.

be direct comparison between experimental and numerical results. Qualitatively, the particle concentrations for the experimental and numerical results can be compared visually, but due to the nature in which the experimental concentration plots were obtained, quantitative values cannot be directly compared.

Figure 20 shows the average velocity profiles of the particle streams prior to impacting with the inclined wall. These comparisons show the influence of the drag model when predicting the particle velocity in a free-falling situation. As the constant stream of particles free-falls, the initially motionless air attempts to retard the particle's motion through the drag force, which in turn imparts velocity of the air in that region, resulting in air movement patterns similar to the particle flow (see Fig. 21). As the air velocity increases, the particles are allowed to travel slightly faster, as the drag force is a result of the relative velocity, and therefore the overall particle velocity increases because the air velocity increases. Effectively freefalling particles are subject to two major forces: gravity, which drives the flow, and drag force, which in this case retards the particles. In terminal velocity cases, the velocity is reached when these two forces balance each other. If the gravity for a given particle or even particle stream remains constant, it can be said that the drag force will also remain constant.

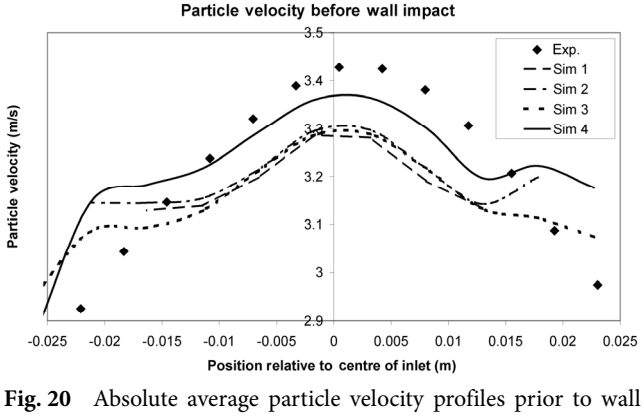

Fig. 20 Absolute average particle velocity profiles prior to wall collision for the large particles at a flow rate of 250 gpm.

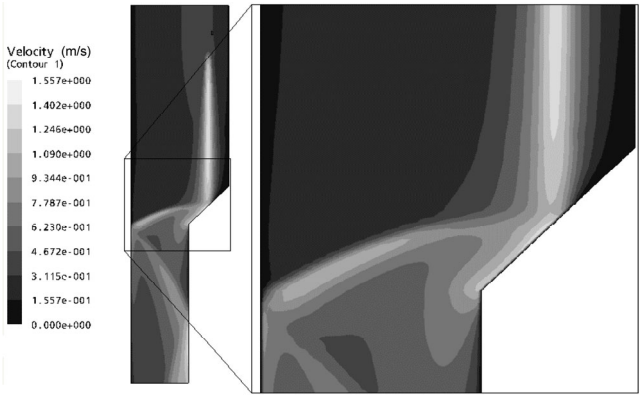

Fig. 21 Gas velocity contour plot for the large particles at the highest flow rebounding off the stainless steel surface.

Therefore, a reduction in the drag coefficient will result in an increase in the relative velocity between the particle and the air.

When considering the behavior of streams of particles opposed to individual particles, the gravity per particle will remain constant as the mass and weight remain constant, but the effective drag force experienced by the particles within the stream will, on average, be smaller, as the effective surface area exposed to air resistance will be smaller, resulting in a reduction in drag force, which in turn leads to higher compensating relative velocity. The velocity comparisons seen in Fig. 20 demonstrate that the inclusion of the new drag model increases the velocities of the predicted particle stream.

The results shown in Fig. 22 are for the normalized post-collision velocities for the large particles at a flow rate of 250 gpm rebounding off the stainless steel surface. The range of the standard CFD model is very small, suggesting that the dispersion of particles is very limited and that all the particles are contained within the main stream. Due to the fact that the post-collision velocities have been normalized against the pre-collision velocities, the effect of the coefficient of restitution can be evaluated, but unless the comparison of pre-collision velocities is given, it is difficult to compare the absolute velocities directly. The normalized values can be somewhat misleading. For different parameters like particle flow rate or rebounding surface roughness, the normalized velocities can be used to compare the trends of the differing parameters, but to directly compare the improvements made in the CFD simulations, the absolute post-collision velocities are required to provide quantitative validation. Figure 23 shows the absolute velocities for the previous case whereby the improvements made by the modified CFD simulation can be seen more clearly. The experimental results predicted higher absolute horizontal velocity, which suggest that the incoming pre-collision velocities were slightly higher due to the fact that the

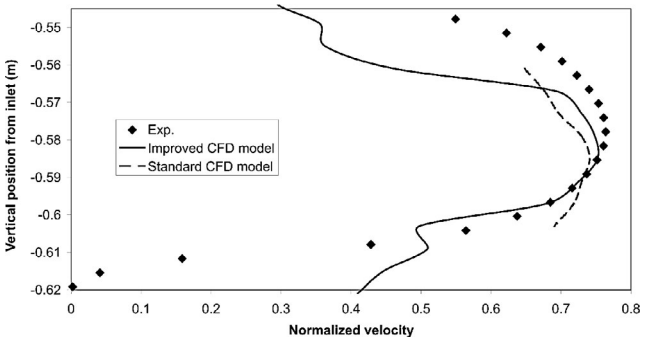

Fig. 22 Normalized horizontal velocities of the large particles at a flow rate of 250 gpm rebounding off the stainless steel surface.

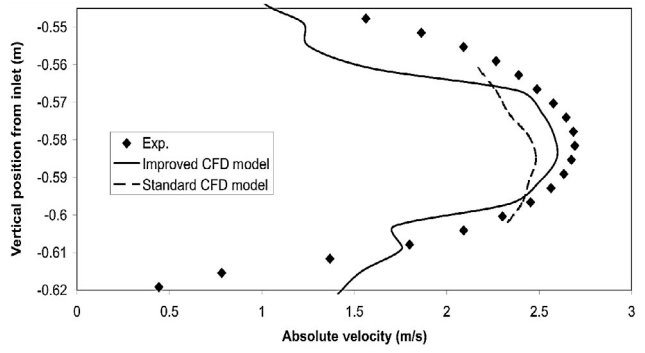

Fig. 23 Absolute horizontal velocities of the large particles at a flow rate of 250 gpm rebounding off the stainless steel surface.

normalized values were very similar. This is confirmed by the drag comparisons shown in Fig. 20 whereby the incoming pre-collision velocities were slightly higher for the experimental results. The increase in the pre-collision velocity seen in the drag comparison for the improved model provides better predictions for particle velocities after the collision process.

It is evident from the experimental findings that a small fraction of particles found themselves outside of the main stream particularly after the collision process; the improved CFD model better predicted this occurrence. Looking at the time-averaged results for the aluminum surface with the large particles at a flow rate of 50 gpm (see Fig. 24), it is clear that again the standard model predicted lower peak velocities within a very narrow band. The improved model did manage to partially predict the spread of particles, but the velocities in the region outside the main stream was somewhat lacking in velocity particularly in the upper region. The peak velocities tended again to show that the new drag model had increased absolute velocities due to higher incoming velocities, which makes sure a better reproduction of the experimental findings.

For the case of the smaller particles, the peak velocities for both CFD models matched very closely with the experimental results, but in this case the peak velocities occurred at points lower than those of the experimental case. In Fig. 25, it can be seen that the peak velocities for the experimental results and CFD predictions were similar. The improved CFD model produced a peak velocity slightly higher than the standard model, more in line with the experimental findings. In the experimental results, the effect of the wall roughness would be more pronounced for the small particles than the larger particles because smaller undulations in the surface will be noticed by the smaller particles. In the CFD simulations, major effect of the wall roughness can only be seen when taking a look at the smaller particles' results. In terms of the presented results, the CFD predictions better matched those of the experimental work, but in truth the particle–wall collision model does not account for the difference in particle size. The authors believe that because the large particles carry a greater velocity into the collision process, the effects of the particle–wall collision models play only a minor role in comparison to the inertial velocity of the larger particles. This is compounded by the improved drag model, which gives the improved CFD simulations higher pre-collision velocities. For all cases, the peak velocity locations differ slightly regarding the larger particles and the difference in the smaller particles are more profound due to their lower overall velocity.

Overall it has been shown that the improved CFD model better predicted the experimental results shown earlier. The improved coefficient of drag force accounts for

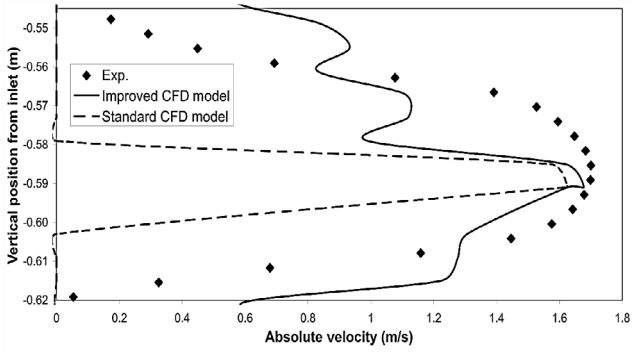

Fig. 24 Absolute horizontal velocities of the large particles at a flow rate of 50 gpm rebounding off the aluminium surface.

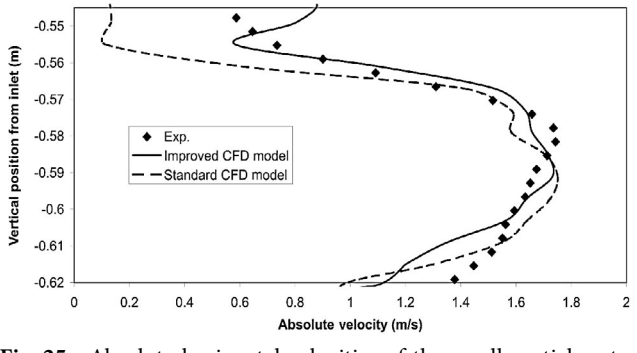

Fig. 25 Absolute horizontal velocities of the small particles at a flow rate of 250 gpm rebounding off the stainless steel surface.

the local particle concentration and the particle Reynolds number. As has been previously shown, a reduced exposed surface area leads to an increase in terminal velocity as the gravity and drag forces balance. The increase in terminal velocity leads to higher incoming pre-collision velocities of the particle streams, which carry through to the absolute post-collision velocities. It is evident from the absolute post-collision velocity results that particularly for larger particles, correctly predicting the incoming velocities, which are primarily governed by the drag force, leads to better agreement in both particle velocity and consequently the mean particle travel path.

7 Conclusions

Experimental measurements and CFD simulations using the Lagrangian approach have been conducted to investigate the flow of particle streams impacting with a 45° inclined surface of differing materials. The main object of the present study was to quantify the behaviour of particle streams under differing mass flow rates and particle sizes. This work was completed to form relevant conclusions on the effectiveness of the standard models in CFX4-4, and to find out whether improving individual models for the drag and particle collisions would indeed improve simulation results. The experimental study may not be groundbreaking, but has been invaluable for testing the improvements made to CFD models and also extends the knowledge base for the behaviour of particle streams, which is distinctly different from individual particles. The experimental results showed that the mass flow rate of the larger particles had very little influence on the normalized velocities post collision, suggesting that the coefficient of restitution remains constant regardless of particle flow rate, as expected. The effect of rebound material on the particle motion was more evident with the larger sized particles whose absolute velocities were higher. It was clearly shown through both the concentration plots and velocity profiles that the stainless steel surface rebounded the particles with a higher velocity, followed by the PVC and lastly the aluminum surface. The results further showed that the new drag model improved the predicted particle velocities within the main particle stream before the collision process and, as a consequence, was able to better predict the post-collision velocities due to the increased speed. Finally, the results have shown that it is impossible to achieve particle distributions like those seen in the experimental work unless a particle–particle collision model is used. The Lagrangian framework basically treats every particle identically, which means the average results will not differ, resulting in a very uniform particle stream before and after the wall collision process. Both CFD models reasonably predicted the mean particle stream motion, but the inclusion of the particle–particle collision definitely gave the concentration plots a visually more qualitative agreement.

Funding note

Open Access funding enabled and organized by CAUL and its Member Institutions.

Declaration of competing interest

The authors have no competing interest to declare that are relevant to the content of this article.

References

Afshar, S., Nath, S., Demirci, U., Hasan, T., Scarcelli, G., Rizvi, I., Franco, W. 2018. Identification of hydrodynamic forces around 3D surrogates using particle image velocimetry in a microfluidic channel. In: Proceedings of the SPIE 10491, Microfluidics, BioMEMS, and Medical Microsystems XVI, San Francisco, California, USA: 9–16.

Clift, R., Grace, J. R., Weber, M. E. 1978. *Bubbles, Drops and Particles*. New York: Academic Press.

Dodds, D., Sarhan, A. R., Naser, J. 2020a. Experimental and numerical study of drag forces on particles in clusters. *Powder Technology*, 371: 195–208.

Dodds, D., Sarhan, A. R., Naser, J. 2020b. Numerical analysis of dilute gas-solid flows in a horizontal pipe and a 90° bend coupled with a newly developed drag model. *Chemical Engineering Research and Design*, 163: 169–181.

Kabeel, A. E., Elkelawy, M., Bastawissi, H. A. E., Elbanna, A. M. 2019. An experimental and theoretical study on particles-in-air behavior characterization at different particles loading and turbulence modulation. *Alexandria Engineering Journal*, 58: 451–465.

Feng, L., Zhang, H., Hu, L., Zhang, Y., Wu, Y., Wang, Y., Yang, H. 2020. Classification performance of model coal mill classifiers with swirling and non-swirling inlets. *Chinese Journal of Chemical Engineering*, 28: 777–784.

Gondret, P., Lance, M., Petit, L. 2002. Bouncing motion of spherical particles in fluids. *Physics of Fluids*, 14: 643–652.

Grant, G., Tabakoff, W. 1975. Erosion prediction in turbomachinery resulting from environmental solid particles. *Journal of Aircraft*, 12: 471–478.

Huber, N., Sommerfeld, M. 1998. Modelling and numerical calculation of dilute-phase pneumatic conveying in pipe systems. *Powder Technology*, 99: 90–101.

Jain, R., Tschisgale, S., Fröhlich, J. 2019. A collision model for DNS with ellipsoidal particles in viscous fluid. *International Journal of Multiphase Flow*, 120: 103087.

Joseph, G. 2003. Collisional dynamics of macroscopic particles in a viscous fluid. California Institute of Technology.

Joseph, G. G., Zenit, R., Hunt, M. L., Rosenwinkel, A. M. 2001. Particle–wall collisions in a viscous fluid. *Journal of Fluid Mechanics*, 433: 329–346.

Kuerten, J. G. M., Vreman, A. W. 2016. Collision frequency and radial distribution function in particle-laden turbulent channel flow. *International Journal of Multiphase Flow*, 87: 66–79.

Li, Z., Miao, Z., Zhou, Y., Wen, S., Li, J. 2018. Influence of increased primary air ratio on boiler performance in a 660 MW brown coal boiler. *Energy*, 152: 804–817.

Luo, K., Zhang, H., Luo, M., Wu, X., Fan, J. 2019. Effects of solid particles and wall roughness on turbulent boundary layer in a two-phase horizontal channel flow. *Powder Technology*, 353: 48–56.

Manjula, E. V. P. J., Ariyaratne, W. K. H., Ratnayake, C., Melaaen, M. C. 2017. A review of CFD modelling studies on pneumatic conveying and challenges in modelling offshore drill cuttings transport. *Powder Technology*, 305: 782–793.

Matsumoto, S., Saito, S. 1970. Monte Carlo simulation of horizontal pneumatic conveying based on the rough wall model. *Journal of Chemical Engineering of Japan*, 3: 223–230.

Miao, Z., Kuang, S., Zughbi, H., Yu, A. 2019. CFD simulation of dilute-phase pneumatic conveying of powders. *Powder Technology*, 349: 70–83.

Muhammad, A., Zhang, N., Wang, W. 2019. CFD simulations of a full-loop CFB reactor using coarse-grained Eulerian–Lagrangian dense discrete phase model: Effects of modelling parameters. *Powder Technology*, 354: 615–629.

Raghav, V., Sastry, S., Saikrishnan, N. 2018. Experimental assessment of flow fields associated with heart valve prostheses using particle image velocimetry (PIV): Recommendations for best practices. *Cardiovascular Engineering and Technology*, 9: 273–287.

Ruiz-Angulo, A., Roshankhah, S., Hunt, M. L. 2019. Surface deformation and rebound for normal single-particle collisions in a surrounding fluid. *Journal of Fluid Mechanics*, 871: 1044–1066.

Shuen, J. S., Solomon, A. S. P., Zhang, Q. F., Faeth, G. M. 1985. Structure of particle-laden jets—Measurements and predictions. *AIAA Journal*, 23: 396–404.

Sommerfeld, M. 1992. Modelling of particle–wall collisions in confined gas-particle flows. *International Journal of Multiphase Flow*, 18: 905–926.

Sommerfeld, M. 2001. Validation of a stochastic Lagrangian modelling approach for inter-particle collisions in homogeneous isotropic turbulence. *International Journal of Multiphase Flow*, 27: 1829–1858.

Sommerfeld, M. 2009. Kinetic simulations for analysing the wall collision process of non-spherical particles. In: Proceedings of ASME 2002 Joint US-European Fluids Engineering Division Conference, Montreal, Quebec, Canada, 2002: 539–547.

Sommerfeld, M. 2003. Analysis of collision effects for turbulent gas-particle flow in a horizontal channel: Part I. Particle transport. *International Journal of Multiphase Flow*, 29: 675–699.

Sommerfeld, M., Huber, N. 1999. Experimental analysis and modelling of particle-wall collisions. *International Journal of Multiphase Flow*, 25: 1457–1489.

Sommerfeld, M., Huber, N., Wächter, P. 1993. Particle-wall collisions: Experimental studies and numerical models. *ASME-PUBLICATIONS-FED*, 166: 183–183.

Sommerfeld, M., Kussin, J. 2003. Analysis of collision effects for turbulent gas-particle flow in a horizontal channel. Part II. Integral properties and validation. *International Journal of Multiphase Flow*, 29: 701–718.

Sommerfeld, M., Kussin, J. 2004. Wall roughness effects on pneumatic conveying of spherical particles in a narrow horizontal channel. *Powder Technology*, 142: 180–192.

Tsuji, Y., Morikawa, Y., Tanaka, T., Nakatsukasa, N., Nakatani, M. 1987. Numerical simulation of gas–solid two-phase flow in a two-dimensional horizontal channel. *International Journal of Multiphase Flow*, 13: 671–684.

Tsuji, Y., Oshima, T., Morikawa, Y. 1985. Numerical simulation of pneumatic conveying in a horizontal pipe. *KONA Powder and Particle Journal*, 3: 38–51.

Varaksin, A. Y. 2019. Collision of particles and droplets in turbulent two-phase flows. *High Temperature*, 57: 555–572.

Westerweel, J. 1997. Fundamentals of digital particle image velocimetry. *Measurement Science and Technology*, 8: 1379–1392.

Zhu, Y., Chen, Y., Xu, Z., Jin, H., Fan, J. 2019. Numerical simulation of gas-particle dense flow with LES/VFDF/SC model. *Computers & Fluids*, 183: 43–52.